

Reconstructing the Direction of Reactor Antineutrinos via Electron Scattering in Gd-doped Water Cherenkov Detectors

D. Hellfeld^{a,*}, A. Bernstein^b, S. Dazeley^{b,**}, C. Marianno^c

^a*Department of Nuclear Engineering, University of California, Berkeley, Berkeley, CA 94720, USA*

^b*Lawrence Livermore National Laboratory, Livermore, CA 94550, USA*

^c*Department of Nuclear Engineering, Texas A&M University, College Station, TX 77843, USA*

Abstract

The potential of elastic antineutrino-electron scattering in a Gd-doped water Cherenkov detector to determine the direction of a nuclear reactor antineutrino flux was investigated using the recently proposed WATCHMAN antineutrino experiment as a baseline model. The expected scattering rate was determined assuming a 13-km standoff from a 3.758-GWt light water nuclear reactor and the detector response was modeled using a GEANT4-based simulation package. Background was estimated via independent simulations and by scaling published measurements from similar detectors. Background contributions were estimated for solar neutrinos, misidentified reactor-based inverse beta decay interactions, cosmogenic radionuclides, water-borne radon, and gamma rays from the photomultiplier tubes (PMTs), detector walls, and surrounding rock. We show that with the use of low background PMTs and sufficient fiducialization, water-borne radon and cosmogenic radionuclides pose the largest threats to sensitivity. Directional sensitivity was then analyzed as a function of radon contamination, detector depth, and detector size. The results provide a list of experimental conditions that, if satisfied in practice, would enable antineutrino directional

*Corresponding author. Tel.: +1 949 680 9345

**Second author. Tel.: +1 925 423 4792

Email addresses: dhellfeld@berkeley.edu (D. Hellfeld), dazeley2@llnl.gov (S. Dazeley)

reconstruction at 3σ significance in large Gd-doped water Cherenkov detectors with greater than 10-km standoff from a nuclear reactor.

Keywords: Reactor antineutrinos, Water Cherenkov detector, Electron scattering, Directionality

1. Introduction

Near-field (< 100 m) monitoring of nuclear reactors via measurements of the antineutrino flux and energy spectrum has been demonstrated using cubic meter scale liquid scintillator antineutrino detectors such as [1–3]. With such measurements, reactor characteristics such as the operational status (on/off), relative power output, and the evolution of the fissionable isotopics in the fuel (burnup) could be determined. The success of these detectors has spurred research in much larger detectors in order to increase both sensitivity and standoff distance [4, 5]. Such detectors could potentially be used as a tool in the nuclear safeguards regime set forth by the International Atomic Energy Agency (IAEA) to reduce the effort needed to conduct physical inspections inside of declared reactor facilities, to monitor facilities in which inspectors do not have access, or to either exclude or search for the presence of clandestine reactors in suspected locations.

Kiloton and megaton scale Gd-doped water Cherenkov antineutrino detectors (WCDs), such as the recently proposed WATER CHerenkov Monitor of ANtineutrinos project (WATCHMAN) [6], are being investigated for medium to long range (> 10 km) remote monitoring of nuclear reactors. These detectors utilize the coincident detection of the positron and neutron from the inverse beta decay (IBD) interaction ($\bar{\nu}_e + p \rightarrow n + e^+$) to determine both the flux and energies of the incident antineutrinos. Water is an attractive option when scaling to such large detector sizes primarily due to both cost and environmental factors; and gadolinium is added (typically 0.1% by weight) to significantly increase both the neutron-tagging efficiency ($\sim 85\%$) and capture energy release (~ 8 MeV). In this work, we analyze whether, in addition to the rate and en-

26 ergy, these detectors can determine the direction of the incident antineutrinos.
 27 Directional sensitivity might prove crucial in instances where multiple reactors
 28 are located nearby, or if a clandestine reactor has been confirmed via the IBD
 29 signal, directionality could be used in conjunction with other measurements,
 30 such as satellite imagery, to determine the location of the reactor. Once the
 31 location is known, other methods could be employed to further characterize the
 32 reactor.

33 Event-by-event reconstruction of the antineutrino direction via IBD in hy-
 34 drogenous media requires knowledge of the neutron momentum vector within a
 35 few recoils following its production. This method of directional reconstruction
 36 has not yet been accomplished for reactor antineutrinos in any medium. In
 37 liquid scintillator detectors, CHOOZ [7] has shown that a partial and stochastic
 38 knowledge of the direction of an incoming antineutrino flux may be gained over
 39 time by reconstructing the relative positions of the positron and neutron ther-
 40 mal capture interaction vertices from an ensemble of IBD interactions. WCDs,
 41 however, presently do not possess the spatial resolution or sensitivity to do this.
 42 In this paper, we investigate whether an alternative interaction, elastic electron
 43 scattering (ES), can be used to determine the direction of a reactor antineutrino
 44 flux incident upon a WCD. The ES interaction ($\bar{\nu}_e + e^- \rightarrow \bar{\nu}_e + e^-$) is highly di-
 45 rectional, meaning the electrons are primarily scattered with a small scattering
 46 angle relative to the incident antineutrino. Thus, in principle, the direction of
 47 the incident antineutrino flux can be determined via directional reconstructions
 48 of an ensemble of scattered electrons.

49 1.1. Antineutrino-electron scattering

50 Neglecting the neutrino mass, the elastic antineutrino-electron scattering
 51 cross-section in the laboratory frame including both the neutral and charged
 52 current components can be written as

$$\begin{aligned}
 53 \quad \sigma(E_{\bar{\nu}_e}) &= \left(\frac{G_F^2 m_e E_{\bar{\nu}_e}}{6\pi} \right) \left[(1 + 2 \sin^2 \theta_W)^2 + 12 \sin^4 \theta_W \right] \\
 54 \quad &\simeq (7.8 \times 10^{-45}) m_e E_{\bar{\nu}_e} \text{ cm}^2 \text{ MeV}^{-2}, \quad (1) \\
 55
 \end{aligned}$$

56 where G_F is the Fermi coupling constant [$= 1.166364 \times 10^{-5} \text{ GeV}^{-2} (\hbar c)^3$] and θ_W
57 is the Weinberg mixing angle ($\sin^2 \theta_W \simeq 0.23$) [8]. Though the ES cross-section
58 is much smaller than IBD, note that the nuclear reactor antineutrino flux is
59 concentrated at low energies, where the interaction cross-section difference is
60 smallest. Water also presents five times as many ES targets as IBD per water
61 molecule ($10 e^-$ vs. 2 quasi-free protons) [see Fig. 1(a)].

62 From energy and momentum conservation in the laboratory frame, it can be
63 shown that the kinetic energy of the scattered electron T_e , is given by

$$64 \quad T_e(\theta, E_{\bar{\nu}_e}) = \frac{2m_e E_{\bar{\nu}_e}^2 \cos^2 \theta}{(m_e + E_{\bar{\nu}_e})^2 - E_{\bar{\nu}_e}^2 \cos^2 \theta}, \quad (2)$$

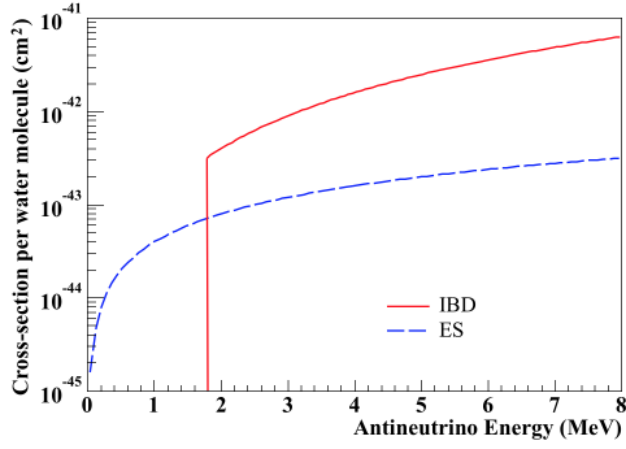
65 where θ is the angle between the incident antineutrino and the scattered electron
66 [8]. Using this, the differential cross-section as a function of the cosine of the
67 scattering angle can be expressed by

$$68 \quad \frac{d\sigma}{d \cos \theta}(\theta, E_{\bar{\nu}_e}) = \frac{4\sigma_0 E_{\bar{\nu}_e}^2 M^2 \cos \theta}{(M^2 - E_{\bar{\nu}_e}^2 \cos^2 \theta)^2} \cdot \left[g_1^2 + g_2^2 \cdot \right. \\
69 \quad \left. \left(1 - \frac{2m_e E_{\bar{\nu}_e} \cos^2 \theta}{M^2 - E_{\bar{\nu}_e}^2 \cos^2 \theta} \right)^2 - \frac{2m_e^2 g_1 g_2 \cos^2 \theta}{M^2 - E_{\bar{\nu}_e}^2 \cos^2 \theta} \right], \quad (3)$$

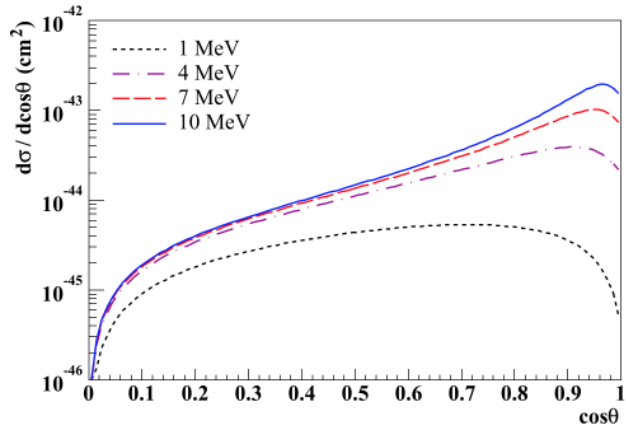
70 where $\sigma_0 = 88.06 \times 10^{-46} \text{ cm}^2$, $M = m_e + E_{\bar{\nu}_e}$, $g_1 = \frac{1}{2}(g_V - g_A)$, and $g_2 =$
71 $\frac{1}{2}(g_V + g_A)$ where g_V and g_A are the weak vector and weak axial-vector coupling
72 constants, respectively [8]. The differential cross-section is plotted in Fig. 1(b)
73 for several incident antineutrino energies. The trend of the cross-section to
74 increase towards $\cos \theta = 1$ reveals that the scattered electrons are primarily
75 scattered in the direction of the incident antineutrinos. Note that the effect
76 becomes more apparent as the incident antineutrino energy increases.

79 1.2. Reactor antineutrino energy spectrum

80 The fission of uranium and plutonium inside of nuclear reactor systems pro-
81 duce neutron-rich fission fragment pairs, which beta decay six times on average
82 before reaching stability. Each one of these decays will produce an antineutrino
83 with a continuum of possible energies. Therefore, experiments and simulations



(a)



(b)

Fig. 1. (Color online) (a) ES and IBD cross-sections per water molecule as functions of incident antineutrino energy. Note the 1.8-MeV energy threshold for IBD. (b) Antineutrino-electron scattering differential cross-section as a function of the cosine of the scattering angle θ .

84 are used to study both the production and subsequent decay of fission products
 85 in critical nuclear reactor systems to understand the reactor antineutrino energy
 86 spectrum. As shown by [9], the number of antineutrinos produced per fission

87 per MeV can be modeled for a particular fissionable isotope by

$$88 \quad \phi(E_{\bar{\nu}_e}) = \exp\left(\sum_{i=0}^2 a_i E_{\bar{\nu}_e}^i\right), \quad (4)$$

89 where the a_i parameters are specific to each isotope. Table 1 displays the fitted
 90 a_i values for the four most dominant fissioning isotopes ($> 99\%$ of all fission)
 91 in nuclear reactors: ^{235}U , ^{238}U , ^{239}Pu , and ^{241}Pu .

92 Though Eq. (4) and Table 1 were determined for reactor antineutrinos rel-
 93 evant to IBD interactions (> 1.8 MeV), it was assumed that Eq. (4) was valid
 94 below this threshold. Our analysis (Section 5) focuses on the high energy do-
 95 main where directionality is strongest, therefore the assumption of extending
 96 the reactor spectrum below the IBD threshold is justified as it will not have
 97 any significant effects on our results. Furthermore, we neglect that the electron
 98 scattering cross-section has been shown to be $\sim 1.5\sigma$ larger than predicted by
 99 the Standard Model at very low energies [9, 10].

Table 1

Parameter values for Eq. (4). The values reported for ^{235}U , ^{239}Pu , and ^{241}Pu are for thermal neutrons and the value for ^{238}U is for 0.5 MeV neutrons [9].

Isotope	a_0	a_1	a_2
^{235}U	0.870	-0.160	-0.0910
^{238}U	0.976	-0.162	-0.0790
^{239}Pu	0.896	-0.239	-0.0981
^{241}Pu	0.793	-0.080	-0.1085

100 The isotopic fissioning concentrations in a nuclear reactor will depend on
 101 the reactor design as well as the level of fuel burnup. In this work, fission
 102 concentrations of a typical mid-cycle pressurized light water reactor (PWR)
 103 were used (49.6% ^{235}U , 35.1% ^{239}Pu , 8.7% ^{238}U , and 6.6% ^{241}Pu) [11]. The
 104 emitted antineutrino energy spectra per fission for each isotope as well as the
 105 summation of the four isotopes weighted by the typical PWR concentrations
 106 are plotted in Fig. 2 with dashed curves. As was mentioned before, reactor
 107 antineutrinos possess relatively low energies, with an average energy of about

108 1.5 MeV. Folding the incident antineutrino energy spectrum with the ES cross-
 109 section results in the observable/detectable spectrum shape in a detector. The
 110 detectable spectra per fission of the four isotopes as well as their weighted
 111 sum are plotted in Fig.2 with solid curves. The average detectable reactor
 112 antineutrino energy is approximately 2.5 MeV.

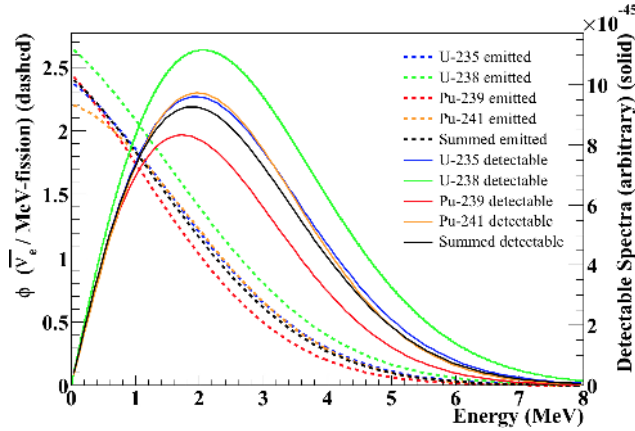


Fig. 2. (Color) Emitted (dashed) and detectable (solid) antineutrino energy spectra per fission from fission occurring in ^{235}U , ^{239}Pu , ^{238}U , and ^{241}Pu . The black lines represent the summation of the four isotopes weighted by the typical fission concentrations of a mid-cycle PWR (49.6% ^{235}U , 35.1% ^{239}Pu , 8.7% ^{238}U , and 6.6% ^{241}Pu).

113 2. The Detector Model

114 For this work we begin by considering a detector design based on the recently
 115 proposed WATCHMAN project [6] - a kiloton scale WCD constructed from a
 116 large cylindrical stainless steel tank [see Fig.3(a)]. The diameter and height
 117 of the cylinder are 15.8 m with a total water volume of about 3.1 kilotons.
 118 Photomultiplier tubes (PMTs) are housed in a cylindrical structure 13.8 m in
 119 diameter, separating the detector into two distinct regions. The outer region
 120 serves as a veto for cosmic muons and the inner region as the target. There
 121 is approximately 2.1 kilotons of Gd-doped water in the target and 1 kiloton
 122 in the veto. The PMT support structure houses approximately 4300 30.48-cm

123 (12-inch) Hamamatsu PMTs facing the target, with photocathode coverage near
124 40%, and 480 PMTs facing the veto. Within the target, a cylindrical fiducial
125 volume (FV) was initially defined with a diameter and height of 10.82 m (\sim 1
126 kiloton). The 1.5 m thick space between the PMT support structure and fiducial
127 volume acts as a buffer region to enable better reduction of backgrounds from
128 the PMTs and external radiation.

129 Like the WATCHMAN detector, the model assumes a single-core 3.758-GWt
130 light water nuclear reactor located 13 km away. To model detector response, a
131 GEANT4 [12] based simulation package named Reactor Monitoring Simulation
132 (RMSim) was used. RMSim is a modified version of WCSim [13], a GEANT4-
133 based program for developing and simulating large WCDs. RMSim contains all
134 relevant physics processes such as particle generation and transport, Cherenkov
135 physics, optical photon production and transport, PMT sensitivity, digitization,
136 and timing. Detailed detector geometry, materials, and optical properties for
137 the WATCHMAN detector are also included. See Fig. 3(b) for a visualization
138 of an antineutrino-electron scattering event in the simulated detector. Event
139 reconstruction was handled by the fitter software code named BONSAI [14],
140 originally developed for the Super Kamiokande (Super-K) experiment. We note
141 that at the time of this writing, BONSAI has not been optimally tuned to the
142 specifications of the proposed detector in the same way as for Super-K.

143 Note that the WATCHMAN detector was not originally designed with ES
144 directional sensitivity in mind. The design was used here as a baseline model
145 simply because a detailed GEANT4-based simulation already existed. Therefore,
146 this work considers modifications to certain features of the detector, namely the
147 size and overburden, that will greatly improve ES directional sensitivity to the
148 reactor antineutrino flux.

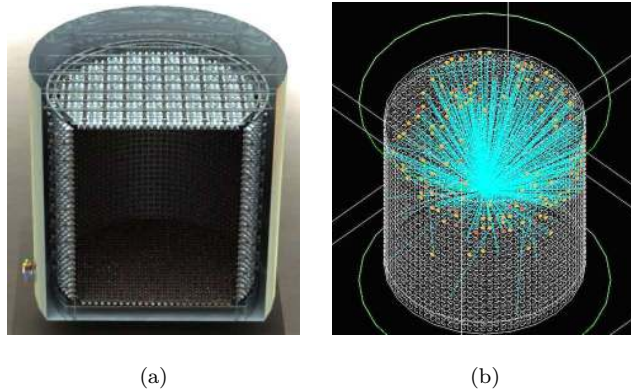


Fig. 3. (Color) (a) Basic design of the proposed kiloton WCD [6]. (b) Visualization of an ES event in the proposed detector modeled in RMSim. The blue lines represent the Cherenkov light and the colored dots represent triggered PMTs.

149 3. Signal

150 Neglecting oscillations, the reactor-based elastic antineutrino - electron scat-
 151 tering rate in a detector can be determined using

$$152 R_{\bar{\nu}_e/e^-} = \frac{N_e}{4\pi D^2} \sum_i f_i \int \phi_i(E_{\bar{\nu}_e}) \sigma(E_{\bar{\nu}_e}) dE_{\bar{\nu}_e}, \quad (5)$$

153 where N_e is the number of available target electrons, D is the reactor-detector
 154 distance (cm), f_i is the fission rate for the particular isotope i (Hz), $\phi_i(E_{\bar{\nu}_e})$
 155 is the number of antineutrinos produced per fission per MeV for isotope i [see
 156 Eq. (4)], and $\sigma(E_{\bar{\nu}_e})$ is the energy dependent scattering cross-section (cm²) [see
 157 Eq. (1)]. The sum runs over the four dominant fissionable isotopes in nuclear
 158 reactors mentioned in Table 1, and the integral runs from 0 to 8 MeV, as in
 159 Fig. 2. Carrying out the calculation with the specifications outlined above results
 160 in about 9270 total scattering events in the kiloton FV over 5 years (not yet
 161 including detector response).

162 An elastic electron scattering generator was developed for RMSim to sim-
 163 ulate the scattered electrons. The generator calculates the total number of
 164 expected interactions for any desired detector size, acquisition time, standoff
 165 distance, reactor power level, and fission isotopics using Eq. (5). It then gener-

166 ates a sample of scattering events by sampling position, energy, and direction
167 using Eqs. (2-4).

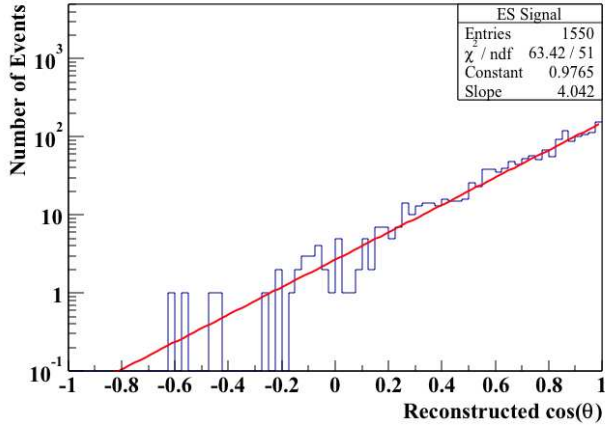
168 Five years worth of ES events were simulated in RMSim and reconstructed
169 using the BONSAI fitter software. The reconstructed cosine of the scattering
170 angles are shown in Fig. 4(a) with a value of $\cos\theta = 1$ denoting a complete
171 forward scatter of the electron. The reconstructed distribution appears to fol-
172 low an exponential-like distribution peaking at $\cos\theta = 1$. RMSim imposes a
173 triggering threshold of 16 photoelectrons, and it can be seen from the plot that
174 only 1550 ($\sim 17\%$) of the original 9270 ES events trigger the detector. Figure
175 4(b) shows the detector response of the triggered ES events in terms of detected
176 photoelectrons. The distribution follows a decreasing exponential that extends
177 to ~ 140 photoelectrons. We note that we expect approximately 10 photoelec-
178 trons/MeV in the detector at low energies. While the PMT coverage is similar
179 (40%), this is slightly larger than the Super-K results of 6 photoelectrons/MeV
180 [15] because of the higher quantum efficiency of the PMTs used here.

181 4. Backgrounds

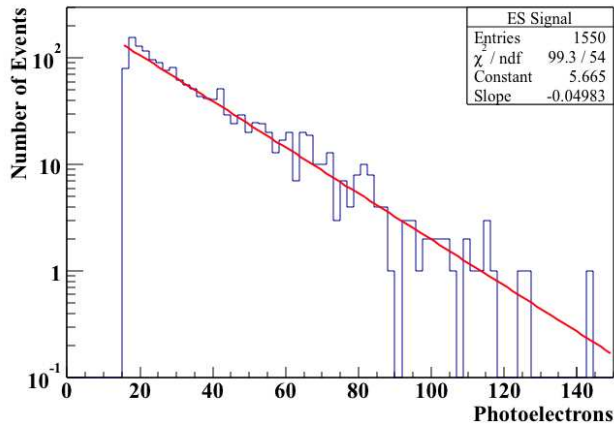
182 Due to the low count rates associated with antineutrino detection, the back-
183 ground levels in the detector must be kept to a minimum to maintain suitable
184 statistics. Several potential sources of background exist for ES including cos-
185 mogenic radionuclides, high-energy gamma rays from the steel vessel and the
186 rock surrounding the detector, solar neutrinos, misidentified IBD events from
187 the reactor, PMT gamma rays, and water-borne radon. All were assumed to be
188 distributed isotropically in direction (neglecting the obvious anisotropy of solar
189 neutrinos). Therefore, in a directional cosine plot, the reactor ES signal should
190 appear as a peak in the forward direction atop a flat background.

191 4.1. Cosmogenic radionuclides

192 Cosmic muons and the hadronic showers they produce can interact with the
193 oxygen atoms in the target region water to create long-lived (> 1 s) radionu-
194 clides. If they beta decay in the inner detector region, the resultant electrons



(a)



(b)

Fig. 4. (Color online) (a) Reconstruction of the cosine of the scattering angle distribution for 5 years of reactor ES in the proposed WCD. (b) Detected photoelectron distribution of the 5-year triggered signal.

195 can trigger the PMTs and mimic the ES signal. The cosmogenic radionuclide
 196 production yields at Super-K have been estimated using FLUKA [16]. Recently,
 197 measurements of the production yields in Super-K were also published [17]. Ta-
 198 ble 2 shows the theoretical and measured results for the five isotopes determined
 199 to be the most relevant for reactor antineutrino-electron scattering due to their
 200 long lifetimes and/or high yields. The theoretical yields were used to determine

201 the production rates in the case of ^{15}C , ^{11}Be , ^8B , and ^8Li because numerical
 202 values were provided for each isotope (the theoretical yields for ^8B and ^8Li
 203 also provide a conservative estimate over the measured values). In the case of
 204 ^{16}N , the measured yield (the larger of the two) was used in the production rate
 205 calculation.

Table 2

Cosmogenic radionuclide production yields in water calculated by [16] and measured by [17] for the Super-K detector. Only the isotopes determined to be relevant to reactor antineutrino-electron scattering are considered.

Isotope	Half-life (s)	Decay Mode	Theoretical Yield ($10^{-7}\mu^{-1}\text{g}^{-1}\text{cm}^2$)	Measured Yield ($10^{-7}\mu^{-1}\text{g}^{-1}\text{cm}^2$)	Primary Process (on ^{16}O)
^{16}N	7.13	$\beta^- \gamma$ (66%), β^- (34%)	18	$23.4 \pm 1.9 \pm 1.7$	(n, p)
^{15}C	2.45	$\beta^- \gamma$ (63%), β^- (37%)	0.8	<3.9	$(n, 2p)$
^{11}Be	13.8	β^- (55%), $\beta^- \gamma$ (45%)	0.8	<10.0	$(n, \alpha + 2p)$
^8B	0.77	β^+	5.8	$4.9 \pm 0.2 \pm 0.2$	$(\pi^+, \alpha + 2p + 2n)$
^8Li	0.84	β^-	13		$(\pi^-, \alpha + ^2\text{H} + p + n)$

206 The production yields of Table 2 can be converted to production rates using

207

$$208 \quad R_i = \rho Y_i L_\mu R_\mu, \quad (6)$$

209 where ρ is the density of the target (g cm^{-3}), Y_i is the yield of isotope i ($10^{-7} \mu^{-1} \text{g}^{-1} \text{cm}^2$),

210 L_μ is the average muon path length in the detector (cm), and R_μ is the muon

211 rate (Hz). To determine how the radionuclide backgrounds scale with depth, we

212 began by assuming a water detector at the Kamioka Liquid scintillator ANTineu-

213 trino Detector (KamLAND) experiment location, which is at the same depth

214 as Super-K. Given the published showering and non-showering muon rates at

215 KamLAND (0.037 Hz and 0.163 Hz, respectively [18]) and the proportion of

216 radionuclides produced by the showering component at this depth is 70% [19],

217 we can use the predictions of Table 2 for water to estimate the radionuclide

218 production rates per unit volume at any depth by scaling with the showering

219 and non-showering muon rates. The total muon rate scaling was obtained from

220 the analytical expression for the differential muon intensity ($\text{cm}^{-2} \text{s}^{-1}$) in the
 221 flat-earth approximation provided by Mei and Hime:

$$222 \quad I_\mu(h_0) = (67.97e^{\frac{-h_0}{0.285}} + 2.071e^{\frac{-h_0}{0.698}}) \times 10^{-6}, \quad (7)$$

223 where h_0 is the vertical depth (km.w.e.) [20]. Similarly, we employed their
 224 expression for the muon energy spectrum for any slant depth (the averaged
 225 distance traveled through rock by muons at an experiment) h (km.w.e.):

$$226 \quad \frac{dN}{dE_\mu} = Ae^{-bh(\gamma_\mu^{-1})} [E_\mu + \epsilon_\mu(1 - e^{-bh})]^{-\gamma_\mu}, \quad (8)$$

227 where A is a normalization constant with respect to the differential muon in-
 228 tensity at a particular depth, $b = 0.4 \text{ km.w.e.}^{-1}$, $\gamma_\mu = 3.77$, $\epsilon_\mu = 693 \text{ GeV}$, and
 229 E_μ is the muon energy in GeV. Once a muon spectrum is generated for an as-
 230 sumed depth, we can calculate the average muon energy. Previously published
 231 estimates of the mean muon energy at KamLAND have ranged from 198 GeV
 232 to 285 GeV [20–22]. A depth of 2350 m.w.e. produces an average muon energy
 233 consistent with the midpoint of the range (240 GeV), and was therefore accepted
 234 as our best estimate of the slant depth of KamLAND. We also make a simpli-
 235 fying assumption that there is an energy above which all muons form showers,
 236 which we define as the “showering equivalent energy”. For KamLAND, where
 237 18% of the muon flux is showering, the “showering equivalent energy” is 354
 238 GeV. Using the same approach and by matching the total muon flux reported
 239 in [23], the depth of the Irvine-Michigan-Brookhaven (IMB) detector site (the
 240 same site for the proposed WATCHMAN detector) was estimated to be 1540
 241 m.w.e. This result is close to the 1570-m.w.e. depth reported by IMB [23].

242 The outer veto is used to identify and reject spallation events following
 243 muons entering the detector. For this work, an additional muon veto must
 244 be applied to reduce cosmogenic radionuclide decays. Following a muon that
 245 traverses the inner FV region, all subsequent events within 2 m of a showering
 246 muon track, or 1 m of a non-showering muon track are removed for a period of
 247 time dependent upon depth. Veto time adjustments as a function of depth are
 248 described in further detail in Section 5.1. The detector live time at each depth

249 was calculated conservatively assuming that all muons traverse the entire length
250 of the cylindrical FV.

251 Applying the tubular veto above, the rate of each of the five major ra-
252 dionuclide components were calculated as a function of depth. Due to its long
253 lifetime and large yield, ^{16}N significantly dominates the mix, producing $\sim 90\%$
254 of the total. Uncertainties in the vertex reconstruction, which result in some
255 radionuclide events being reconstructed outside the tubular veto regions sur-
256 rounding the muon tracks, were also determined via independent simulations
257 and included in the calculations.

258 *4.2. PMT gamma rays*

259 The PMT glass will contain trace amounts of natural U, Th, and K. The
260 decays of ^{208}Tl (from the Th decay chain) and ^{40}K will produce 2.6-MeV and
261 1.4-MeV gamma rays, respectively. Most of these will interact outside the FV,
262 but due to the uncertainty in the event reconstruction, some events will be
263 reconstructed inside, contributing to the background. An arbitrary number of
264 PMT gamma rays were simulated in RMSim and the black curve (right diagonal
265 shading) in Fig. 5 shows the distance from the reconstructed interaction vertex
266 to the nearest PMT for each event. From the figure, it is clear that a significant
267 number of events are reconstructed inside the FV (> 150 cm away from the
268 PMTs), forming two distinct groups. Near the PMTs, the black curve appears
269 to follow an exponential, whereas further away from the PMTs an almost flat
270 distribution is observed. To improve upon the results, we attempt to remove
271 the poorly fit events. By applying a cut to the log likelihood fit parameter
272 (≥ 25) and the number of triggered PMTs (≥ 25), roughly half of the events
273 are removed, leaving an exponential distribution with respect to the distance to
274 the PMTs (shown in blue and left diagonal shading in Fig. 5).

275 The exponential behavior of the blue curve (left diagonal shading) in Fig. 5 is
276 a promising result, if realizable in practice. It implies that the PMT gamma ray
277 background can be reduced to a subdominant level with a large enough buffer
278 region. To reduce the PMT gamma ray backgrounds with a fixed detector size

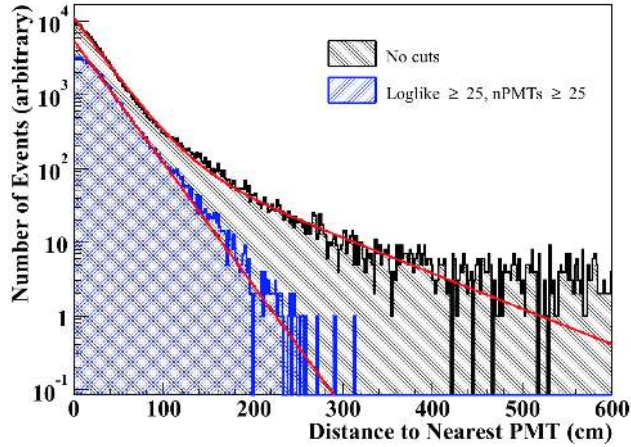


Fig. 5. (Color online) PMT-based background events as a function of the distance from the reconstructed vertex to the nearest PMT (black and right diagonal shading). The blue curve (left diagonal shading), which requires both the triggered PMT count (nPMTs) and the log likelihood (Loglike) to be ≥ 25 , follows an exponential distribution.

279 however, the FV must be decreased to allow for a sufficient buffer thickness. This
 280 will result in a significant reduction in the number of detectable ES interactions.
 281 Assuming an exponential distribution with respect to distance from the PMTs,
 282 the PMT gamma ray background can be estimated for any sized FV using the
 283 assumed impurity levels of Th and ^{40}K in the glass. In this work, the PMTs
 284 are assumed to have similar radioactivity levels as the low-background 25.4-cm
 285 (10-inch) Hamamatsu PMTs employed at the Double CHOOZ detector with Th
 286 and ^{40}K impurity concentrations of 0.03 ppm and 20 ppm, respectively [24].

287 4.3. Water-borne $^{222}\text{Rn}/^{214}\text{Bi}$

288 The beta decay of ^{214}B (a daughter product of the ^{238}U decay chain prod-
 289 uct ^{222}Rn , $Q = 3.3$ MeV) in the target region will also contribute a significant
 290 amount of background to the ES signal. The presence of $^{222}\text{Rn}/^{214}\text{Bi}$ in the
 291 water can occur due to a variety of processes. Some may result due to trace
 292 amounts of naturally occurring ^{238}U present in the water, dissolved ^{222}Rn that
 293 has migrated out of the PMT glass, and from radon gas entering the detec-
 294 tor from the mine air. The Sudbury Neutrino Observatory (SNO) heavy water

295 neutrino detector has reported an inner detector radon contamination of 10^{-14}
296 gU/gD₂O, assuming the U is in secular equilibrium with ²²²Rn [25]. Assuming
297 this level of contamination in the proposed light water detector results in about
298 about 10^4 ²¹⁴Bi decays per day somewhere in the 1000-m³ FV, of which ap-
299 proximately 20% survive the GEANT4 detector simulation trigger condition (16
300 photoelectrons).

301 Actual radon levels achievable in a real detector will rely on the water recir-
302 culation methods employed, as well as the radon concentration in the mine air,
303 both of which could be significantly different than SNO. The SNO detector also
304 employs an acrylic barrier between the heavy water target and the light water
305 buffer. The acrylic, while it impedes the migration of radon from the PMTs to
306 the target, might also be a mild source of radon. One might envision a different
307 water flow scheme, in which radon free fresh water is injected inside the target
308 and directed outward via positive pressure, could achieve reductions in radon
309 contamination relative to SNO. In this work, since it is difficult to predict phys-
310 ically achievable radon concentrations, we simply assume similar concentrations
311 to SNO as well as hypothetical situations in which the radon contamination can
312 be reduced further.

313 *4.4. Other backgrounds*

314 The backgrounds due to gamma rays from the detector steel vessel and
315 the surrounding rock were determined using a study performed by the Isotope
316 Decay At Rest (IsoDAR) collaboration on the KamLAND detector [26]. IsoDAR
317 assumed a 5-m sphere FV at KamLAND, thus the results from [26] were scaled
318 to account for the much larger cylindrical FV of the proposed detector (1000
319 m³). Specifically, the estimates were scaled using the difference in the fiducial
320 surface areas. This method assumes the proposed detector steel vessel will have
321 similar cleanliness levels as KamLAND and the surrounding rock will be of
322 similar composition to the KamLAND mine. The differences in densities and
323 gamma attenuation lengths between the scintillator used in KamLAND and the
324 water used in the detector under study, as well as the differences in gamma path

325 lengths for the spherical and cylindrical geometries were neglected. All gamma
326 rays that reached the FV were assumed to interact.

327 The ^8B solar neutrino background was also determined by scaling from [26].
328 Assuming the neutrino flux is constant with depth, the interaction rate is de-
329 pendent solely on the number of available targets, which is proportional to the
330 fiducial mass. Therefore the solar neutrino background estimation in [26] was
331 scaled according to the difference in the the KamLAND fiducial mass (0.408
332 kilotons) and the proposed detector fiducial mass (1 kiloton).

333 The scaled steel, rock, and solar neutrino results from [26] were corrected for
334 the difference in detector live time between KamLAND (56.2%) and the model
335 at any depth. Corrections were also included to account for the 3-MeV visible
336 energy threshold used in [26].

337 If the neutron from a reactor-based IBD event is not detected within the
338 time or spatial coincidence requirements, or it is simply not captured, then the
339 lone positron signal will mimic ES. These misidentified IBD backgrounds were
340 estimated assuming an IBD interaction rate of 20 events per day and a 20%
341 missed neutron rate as in [6].

342 5. Analysis

343 As mentioned in Section 4, background events are assumed to be isotropic
344 in direction. Reconstructed ES signal events exhibit an exponential behavior
345 towards $\cos\theta = 1$. Therefore, in a plot of the cosine of the scattering angle, we
346 expect the total signal to follow the behavior of a constant plus an exponential
347 curve as in

$$348 \quad y = A + Be^{Cx}, \quad (9)$$

349 where A , B , and C are free parameters in the fit to the data. To determine
350 the statistical significance of the ES signal, an arbitrarily large independent
351 sample of ES events was simulated to determine the exponential slope param-
352 eter C . With the slope parameter fixed, the uncertainty in the exponential

353 normalization parameter B was used to determine the uncertainty and statis-
 354 tical significance of the signal. This analysis method would only be possible in
 355 practice if the exponential slope could be obtained *a priori* using directional
 356 calibrations, such as the electron accelerator at Super-K [27].

357 Figure 6 displays the detector response (photoelectron production) from all
 358 sources of background except PMTs, as well as the ES signal for a time pe-
 359 riod of one year in a 3-kiloton water detector at the depth of the KamLAND
 360 detector (2350 m.w.e.). PMT backgrounds were not included because the rate
 361 normalization, which ranges from dominant to minor, depends entirely on the
 362 arbitrary fiducial volume chosen. From the plot it is clear that $^{222}\text{Rn}/^{214}\text{Bi}$
 363 dominates the total number of backgrounds, particularly at low energies. At
 364 higher energies and shallower depths, radionuclides begin to dominate.

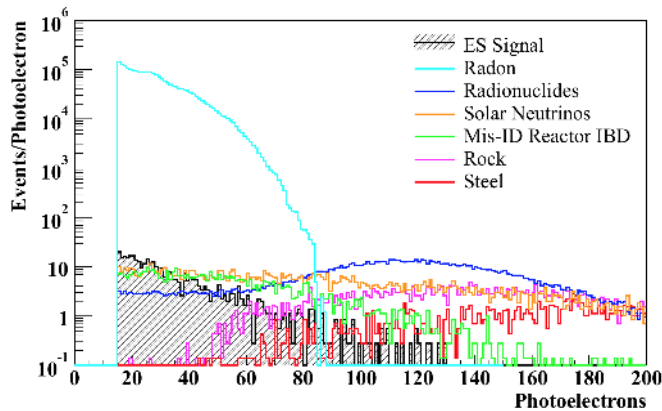


Fig. 6. (Color) The most significant backgrounds expected in a kiloton FV WATCHMAN-like detector over a one-year data acquisition period together with the ES signal at the same depth as KamLAND (2350 m.w.e.). Water-borne $^{222}\text{Rn}/^{214}\text{Bi}$ and cosmogenic radionuclides represent the most important background types shown here. Note, sufficient distance between the PMTs and the fiducial volume was assumed to reduce PMT backgrounds to a subdominant level. In the following, we investigate the sensitivity of our model to many of these backgrounds as a function of energy, depth, and fiducial volume.

365 Based on the spectral shapes shown in Fig. 6, it is worth investigating if
 366 detector sensitivity has some dependence on the amount of detected energy.
 367 First, note that the ES shape extends to higher energies than the radon back-

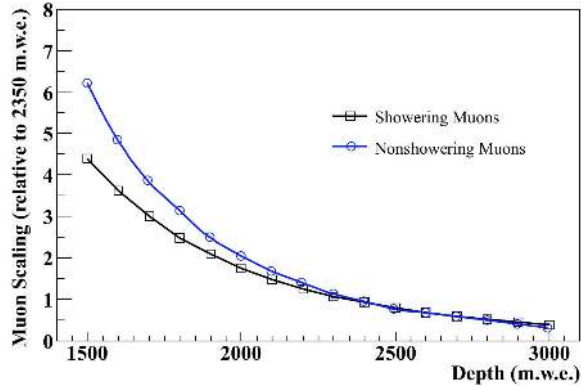
368 ground. The radionuclide background, however, begins to dominate at high
369 energy. Therefore, in the following section, detector sensitivities are presented
370 for small slices in energy ($25 \rightarrow 65$ and $60 \rightarrow 90$ triggered PMTs) and at differ-
371 ent depths. At higher energies, the PMT based backgrounds are both lower in
372 number and more accurately reconstructed, and thus larger FVs can be used.
373 For the radon, it is clear that a significant improvement in contamination (rel-
374 ative to the SNO levels) would need to be made before ES directionality might
375 be achievable. We cannot comment on whether a dedicated R&D campaign
376 or a new scheme of optimized water flow might be able to achieve significant
377 improvements. Here we simply calculate the sensitivities that would result if
378 significant reductions were achieved.

379 *5.1. Sensitivity vs. depth*

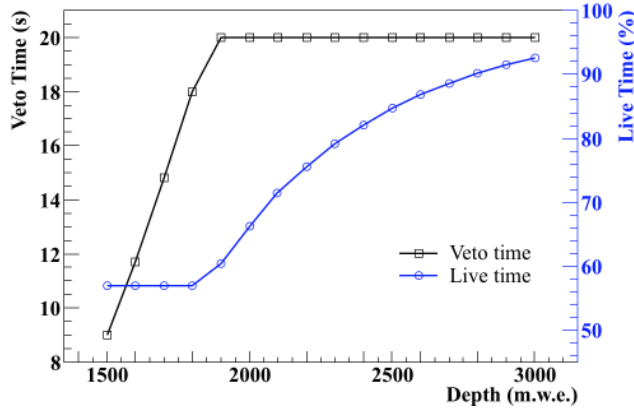
380 We now investigate the overall behavior of the directional sensitivity as a
381 function of depth using the showering and non-showering muon rate scalings
382 with depth determined with the methods described in Section 4.1. For the
383 purpose of this work, we only consider depths from 1500 to 3000 m.w.e. The
384 showering and non-showering scaling factors (relative to the KamLAND depth)
385 are shown in Fig. 7(a).

386 Using the muon scalings, the radionuclide background and detector live time
387 were determined as a function of depth. Because the muon rate decreases signif-
388 icantly with depth, the position sensitive veto time can be increased to remove
389 more radionuclide background without suffering any live time losses. There-
390 fore, the tubular veto time was increased with depth to maintain a live time
391 approximately equal to the KamLAND live time (56%). A maximum veto time
392 of 20 s was arbitrarily imposed since the radionuclides will migrate outside of
393 the tubular veto if given enough time. Figure 7(b) displays the veto times and
394 detector live times as a function of depth used in subsequent calculations. A
395 veto time of 20 s is reached at 1900 m.w.e. and remains fixed at deeper depths.

396 The average statistical significances as a function of depth and radon con-
397 tamination relative to SNO were then determined. The results are shown in



(a)



(b)

Fig. 7. (Color online) (a) Showering and non-showering muon rates as a function of depth (relative to KamLAND) determined from [20]. (b) Veto times used in the position sensitive veto system as a function of depth and the resultant detector live times. The veto time was varied as a function of depth in order to retain a constant live time up to a maximum veto time of 20 s, which was reached at 1900 m.w.e.

398 Fig. 8 for radon levels of $1 \times \text{SNO}$ [Fig. 8(a)], $10^{-2} \times \text{SNO}$ [Fig. 8(b)], and $10^{-4} \times$
 399 SNO [Fig. 8(c)]. As an example, Appendix A displays a detailed breakdown of
 400 the expected number of elastic scattering signal and background events in the
 401 two different energy ranges for a kiloton sized WATCHMAN-like detector at the
 402 same depth as KamLAND (2350 m.w.e.). Repeated multiple independent data
 403 samples were used to calculate the mean significance per 5-year experiment.

404 Error bars are included in Fig. 8(a)-(c) and represent the uncertainty in the
405 mean of the many independent 5-year experiments, however are too small to be
406 observed here. Note, the results of a single experiment will produce sensitivity
407 values distributed around the mean with an uncertainty of approximately 1σ .
408 With no reduction in radon (relative to SNO), directionality does not seem to
409 be possible at any depth with a kiloton sized detector. If the radon contami-
410 nation is significantly reduced (by four orders of magnitude), the $25 \rightarrow 65$ slice
411 produces the most significant signal. This is clearly observed in Fig. 8(c), where
412 a 3σ significance can be obtained using this slice starting at about 1900 m.w.e.

413 The total detector size (including the fiducial, buffer, and veto) required to
414 obtain a significant (3σ) signal was also considered for the three radon levels
415 in Fig. 8(a)-(c). This was done assuming both the signal and background scale
416 linearly with the FV, while significance scales with the signal (S) to background
417 (B) ratio (S/\sqrt{B}). The respective buffer and veto thicknesses for each energy
418 range were then added to determine the total detector size. The results are
419 shown in Fig. 8(d)-(f) for all three radon levels. Error bars are included and
420 represent the uncertainties in Fig. 8(a)-(c) propagated through the calculation.
421 However, once again, the error bars represent the uncertainty in the mean and
422 do not represent the uncertainty of a single experiment.

423 If in fact radon levels cannot be reduced relative to SNO, the detector size
424 needs to be increased significantly (> 50 kilotons) in order for directionality to be
425 possible. If significant radon reduction is possible, detector sizes anywhere from
426 3 kilotons (WATCHMAN-size) to 10 kilotons may be directionally sensitive,
427 depending on the specific depth and radon levels.

428 6. Conclusions

429 Our study shows that under certain conditions, the reconstruction of the
430 direction of a reactor may be achievable via the antineutrino-electron scatter-
431 ing channel. The main factors affecting sensitivity are radon contamination
432 and overburden. With similar water-borne radon levels to SNO and a 3000-

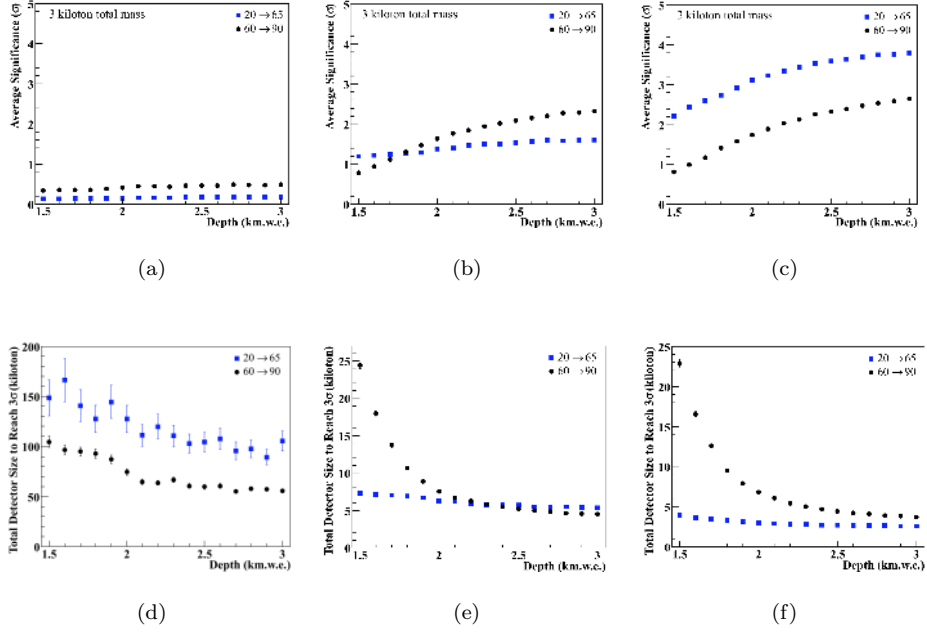


Fig. 8. (Color) Average statistical significance in a 3-kiloton detector (total mass) plotted as a function of depth using two different energy ranges considered here (25 to 65 and 60 to 90 hit PMTs), with radon levels of $1 \times \text{SNO}$ (a), $10^{-2} \times \text{SNO}$ (b), and $10^{-4} \times \text{SNO}$ (c). Error bars are included and represent the uncertainty in the mean (however they are too small to be seen in most cases). The uncertainty in a single experiment is $\pm 1\sigma$. Total detector size required for 3σ significance plotted as a function of depth for radon levels of $1 \times \text{SNO}$ (d), $10^{-2} \times \text{SNO}$ (e), and $10^{-4} \times \text{SNO}$ (f). Again, error bars represent the uncertainty in the mean and do not represent the uncertainty in a single experiment. Therefore the results should only be used as a guide.

433 m.w.e. depth, a fairly large detector approximately the size of Super-K (55-
 434 kiloton total, 37-kiloton fiducial) is required for 3σ sensitivity to the assumed
 435 3.758-GWt reactor at 13-km standoff. With a factor of 100 radon reduction and
 436 at least 2000-m.w.e. depth, a more tractable 6.3-kiloton (885-ton fiducial) detec-
 437 tor is sufficient for the same reactor power and significance level (see Appendix B
 438 for an example of a directional plot with these conditions). If a significant re-
 439 duction in radon is possible ($10^{-4} \times \text{SNO}$), a 4-kiloton (172-ton fiducial) detector
 440 at a shallower 1500-m.w.e. depth (similar to WATCHMAN) would be direction-

441 ally sensitive for the same reactor power and significance level. Assumptions in
442 these results include similar steel cleanliness levels to the KamLAND detector, a
443 continuously operated reactor at full power with no shutdown periods, and con-
444 stant fission fractions typical of a mid-cycle PWR. Furthermore, the situation
445 investigated here is the directional sensitivity of an incoming antineutrino flux
446 with respect to an assumed reactor location. If the true location is unknown, a
447 statistical penalty would need to be applied for testing in multiple directions.

448 More generally, flux scaling allows us to approximate directional sensitivity
449 at greater distances and for smaller reactor power levels. Assuming the case
450 of $10^{-2} \times$ SNO radon contamination and 2500-m.w.e. overburden, directional
451 reconstruction of a 3.758-GWt reactor at 3σ significance would be possible at a
452 70-km standoff with a 1-megaton (757-kiloton fiducial) detector. Equivalently,
453 a megaton detector would be sensitive to a 125-MWt reactor at 13 km. If
454 the radon contamination is reduced by 10^4 , the 3.758-GWt reactor standoff
455 increases to 105 km while the smallest detectable reactor at 13 km decreases
456 to 55 MWt. Megaton-sized water-based detectors represent the outer limit of
457 what is possible in field-able neutrino detectors [28].

458 While these conditions may be difficult to achieve in practice, we have
459 demonstrated that Gd-doped WCDs have the potential to utilize elastic elec-
460 tron scattering for nuclear reactor antineutrino directionality. Compared with
461 the WATCHMAN detector, the main factors for improvement in directional
462 pointing are greater depth and 10^{-2} or less radon contamination in the inner
463 detector volume compared with the SNO detector. We hope that this research
464 may serve as a catalyst to pursue an R&D effort into water-borne radon removal
465 techniques for future large scale Gd-doped WCDs used for remote monitoring
466 of nuclear reactors.

467 **Acknowledgements**

468 The authors would like to thank Marc Bergevin of Lawrence Livermore
469 National Laboratory for his help with the development and usage of RMSim

470 for the purposes of this work and Michael Smy of the University of Califor-
471 nia, Irvine for his assistance with BONSAI. This work was supported by the
472 U.S. Department of Energy National Nuclear Security Administration [Award
473 No. DE-NA0000979] through the Nuclear Science and Security Consortium, and
474 Lawrence Livermore National Laboratory [Contract No. DE-AC52-07NA27344,
475 LDRD tracking number 15-ERD-021, release number LLNL-JRNL-679610]. The
476 views and opinions of authors expressed herein do not necessarily state or reflect
477 those of the United States Government or any agency thereof.

478 **Appendix A. Example: Signal and Background Estimates at Kamioka** 479 **Depth**

480 Table 3 shows the predicted number of reactor-induced elastic scattering
481 events 13 km from a 3.758-GWt power reactor, and the expected number of
482 background events after 5 years in a WATCHMAN-like detector at the same
483 depth as the KamLAND detector (2350 m.w.e.). “WATCHMAN-like” refers
484 to a 0.1% Gd-doped water Cherenkov detector with a total detector volume of
485 just over 3 kilotons, a 2-kiloton inner detector volume and a nominal 1-kiloton
486 fiducial volume. The actual fiducial volume depends on the energy cuts used.
487 The two energy regimes used here extend from 25 to 65 triggered PMTs and
488 from 60 to 90 triggered PMTs. The table also includes the fixed exponential
489 slope used in Eq. (9) and the average statistical significance for the three different
490 assumed radon contaminations relative to the SNO detector.

Table 3

Signal and background estimates for a WATCHMAN-like detector at a depth of 2350 m.w.e for 5 years assuming two different energy analysis cuts. Average significances were calculated assuming the radon levels relative to those of SNO. The radionuclide background is denoted by “RN” and the backgrounds due to steel, rock, misidentified IBD, and solar neutrinos are combined together and denoted by “Other”. Since the ideal FV can change with increasing energy, we include the range of FVs used within each energy slice.

5 Year Acquisition										
PMT Triggers	FV (m ³)	ES	Exp. Slope		RN	PMTs	Other	Radon (\times SNO)		
								1	10 ⁻²	10 ⁻⁴
25 \rightarrow 65	187	97	4.6	Bkgd. Components	123	1463	511	1148920	11489	115
				Total Background				1151017	13586	2212
				Significance				0.1 σ	1.5 σ	3.5 σ
60 \rightarrow 90	500 - 1000	51	6.7	Bkgd. Components	722	270	1278	61485	615	6
				Total Background				63755	2885	2276
				Significance				0.5 σ	2.0 σ	2.2 σ

491 **Appendix B. Example: Directional Signal and Background Plot**

492 Figure 9 shows an example 5-year directional reconstruction of all signal
 493 and background events that trigger between 25 and 65 PMTs in a 6.3-kiloton
 494 (885-ton fiducial) detector at a depth of 2000 m.w.e. with radon contamination
 495 reduced by a factor of 100 relative to SNO. These conditions represent a more
 496 tractable experimental design option to achieve a 3 σ directional signal with
 497 respect to an assumed known direction.

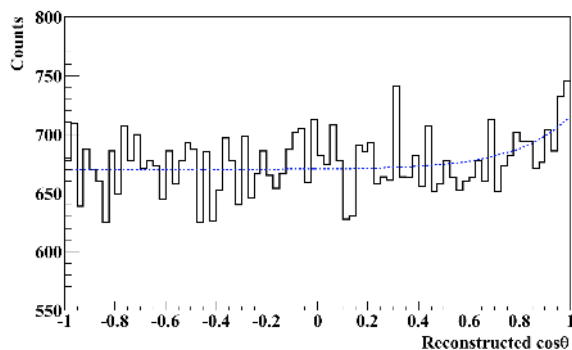


Fig. 9. (Color online) Cosine of the reconstructed angle for all low-energy (25 to 65 triggered PMTs) events in 5 years for a 6.3-kiloton (885-ton fiducial) detector at a depth of 2000 m.w.e. with a radon level of $10^{-2} \times \text{SNO}$. The exponential fit shown in blue has a fixed slope of 4.6 as in Table 3. The directional significance of the antineutrino source at $\cos \theta = 1$ from this particular data is 3.1σ .

References

- 498
- 499 [1] N. S. Bowden, et al., Nucl. Instrum. Methods A 572 (2007) 985.
- 500 [2] L. Mikaelyan, in: Proceedings of the International Conference “Neutrino
501 77”, Vol. 2, Nauka, Moscow, 1978, pp. 383–385.
- 502 [3] A. Bernstein, N. S. Bowden, A. Misner, T. Palmer, J. Appl. Phys. 103
503 (2008) 074905.
- 504 [4] A. Bernstein, G. Baldwin, B. Boyer, M. Goodman, J. Learned, J. Lund,
505 D. Reyna, R. Svoboda, Science & Global Security 18 (3) (2010) 127–192.
- 506 [5] T. Lasserre, M. Fechner, G. Mention, R. Reboulléau, M. Cribier, A. Le-
507 tourneau, D. Lhuillier, arXiv:11011.3850.
- 508 [6] A. Bernstein, et al., arXiv:1502.01132.
- 509 [7] M. Apollonio, et al., Phys. Rev. D 61 (1999) 012001.
- 510 [8] C. Giunti, C. W. Kim, Fundamentals of Neutrino Physics and Astrophysics,
511 Oxford University Press, Oxford, 2007.

- 512 [9] P. Vogel, J. Engel, Phys. Rev. D 39 (1989) 3378.
- 513 [10] Amsler, et al., Phys. Lett. B 545 (2002) 57–61.
- 514 [11] G. Zacek, et al., Phys. Rev. D 34 (1986) 2621.
- 515 [12] S. Agostinelli, et al., (GEANT4 Collaboration), Nucl. Instrum. Methods A
516 506 (2003) 250.
- 517 [13] The Water Cherenkov Simulator (WCSim). Repository:
518 <https://github.com/WCSim>.
- 519 [14] M. Smy, in: Proceedings of the International Cosmic Ray Conference, Vol.
520 5 (HE part 2), Mexico City, Mexico, 2008, pp. 1279–1282.
- 521 [15] A. Renshaw, et al. (Super-K Collaboration), Phys. Rev. Lett 112 (091805).
- 522 [16] S. W. Li, J. F. Beacom, Phys. Rev. C 89 (2014) 045801.
- 523 [17] Y. Zhang, et al. (Super-K Collaboration), Phys. Rev. D 93 (2016) 012004.
- 524 [18] S. Abe, et al. (KamLAND Collaboration), Phys. Rev. C 84 (2011) 035804.
- 525 [19] S. Abe, et al. (KamLAND Collaboration), Phys. Rev. C 81 (2010) 025807.
- 526 [20] D. M. Mei, A. Hime, Phys. Rev. D 73 (2006) 053004.
- 527 [21] T. Hagner, R. von Hentig, B. Heisinger, L. Oberauer, S. Schönert, F. von
528 Feilitzsch, E. Nolte, Astroparticle Physics 14 (2000) 33–47.
- 529 [22] C. Galbiati, J. F. Beacom, Phys. Rev. C 72 (025807).
- 530 [23] R. Becker-Szendy, et al., Nucl. Instrum. Methods A 324 (1993) 363–382.
- 531 [24] J. Felde, (private communication), Internal LBNE DocDB document num-
532 ber 729-v1 (2010).
- 533 [25] I. Belvis, et al., Nucl. Instrum. Methods A 517 (2004) 139–153.
- 534 [26] J. M. Conrad, M. Shaevitz, I. Shimizu, J. Spitz, M. Toups, L. Winslow,
535 Phys. Rev. D 89 (2014) 072010.

⁵³⁶ [27] Y. Koshio, Ph.D. thesis, University of Tokyo.

⁵³⁷ [28] S. Abe, et al. (Hyper-K Working Group), arXiv:1109.3262.